ACS AUTHORCHOICE Article

CRYSTAL GROWTH & DESIGN

Cite This: Cryst. Growth Des. 2019, 19, 5249−5257

pubs.acs.org/crystal

Evolution of Anodic Product from Molybdenum Metal in Absolute Ethanol and Humidity Sensing under Ambient Conditions

Chengsheng Ni,*[,†,‡,§] Darragh Carolan,[‡] Jianing Hui,[§] Conor Rocks,[‡] Dilli Padmanaban,[‡] Jiupai Ni,[†] Deti Xie,[†] Zeguo Fang,[§] John Irvine,[§] Paul Maguire,[‡] and Davide Mariotti[‡]

[†]College of Resources and Environment, Southwest University, Beibei, Chongqing 400716, China

[‡]School of Engineering, Ulster University, Jordanstown Campus, Shore Road, Newtownabbey, Northern Ireland, BT37 0QB, United Kingdom

[§]School of Chemistry, University of St. Andrews, Fife, Scotland, KY16 9ST, United Kingdom

Supporting Information

ABSTRACT: Room-temperature nonaqueous synthetic routes turn out to be particularly competitive among all the available liquid-phase synthetic methods for nanometer-sized metal oxides for multiple applications. Microplasma-assisted anodization is employed to prepare soluble and crystalline Mo species in a water-deficient and extraneous ionic-salt-free ethanol electrolyte. The anodization of Mo in absolute ethanol is found to produce Mo oxyethoxide in the liquid ethanol phase, along with a small montage of mixed hexagonal and orthorhombic MoO_3 crystals. The evolution of Mo species in solid and liquid phases is characterized to study the crystallization of MoO_3 crystal and the formation of blue spherical Mo polyoxometalates (POMs) after extended aging. The addition of water in the suspension delayed the formation of molybdenum blue while hydrogen peroxide induced the precipitation of a dendritic framework of hexagonal MoO_3. A thin MoO_3 film was produced from the solution and can be used for humidity sensing by the facile conductivity measurement.

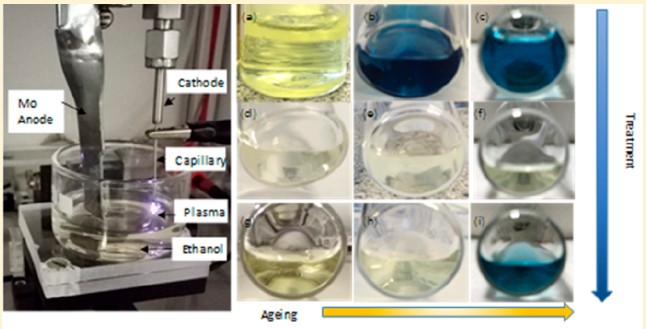

INTRODUCTION

The rapid growth of inorganic nanoparticles prepared by nonaqueous and/or nonhydrolytic processes clearly indicates that synthesis in organic solvents under the exclusion of water is a versatile alternative to aqueous methods.[1] However, the liquid-phase routes employed to date, even with organic solvent, including coprecipitation, sol−gel process, solvothermal. etc., require a final calcination at moderate temperature to remove the organic material or increase the crystallinity of the inorganic material,[2] and the rational synthesis of crystalline materials at room temperature and ambient pressure is still a prominent challenge.[2,3] Recently, hybrid microplasma-liquid electrochemical systems under ambient conditions have been demonstrated as an efficient and green method for the synthesis of nanoparticles, such as metals,[4,5] metal oxides,[6−8] polymers,[9,10] etc. MoO_3 nanocrystals in suspension for the processing of thin films or highly efficient catalyst[11] are often prepared via wet-chemical strategies, such as hydrothermal synthesis or temperature-controlled reflux,[12,13] where molybdate and heating steps are required to control the structure and morphology of the products. The anodization of molybdenum metal in aqueous solution is generally unattainable, because the anodization potential is higher than the oxidation of water and a stable and protective oxide film is formed on the surface of the electrode.[14−16] In contrast, a blue MoO_x film was deposited on F-doped SnO_2 (FTO) film from a electrolyte of Na_2MoO_4 at different pHs and this could be related to the reduction of Mo^{VI} species.[17] The use of absolute ethanol would be a viable method to avoid the use of aqueous electrolytes or hydrated molybdate, since the production of ionic species from ethanol under the microplasma would provide the charge carriers for the electrochemical reaction.[6,18]

Sensors are widely used in environmental monitoring, industrial/agricultural production, and daily lives[19−21] and sensors based on nanosized metal oxides, such as SnO_2, CeO_2, and perovskites, are popular ones for humidity sensing.[22−25] MoO_3 has been used in the humidity sensing of trimethylamine,[26,27] ammonia,[28] ethanol,[29] volatile organic compounds (VOCs),[30,31] and hydrogen,[17,31] but it can also be used for humidity sensing, using the facile resistivity technique.[32−38] The α-MoO_3-based humidity sensor has been prepared via the evaporation of Mo^0 under an O_2 atmosphere,[33,34] and MoO_3 plays a major role in enhancing the humidity sensing performance of composites due to the variation of microstructure[37] and the water adsorption kinetics in the composite sensor with oxides[32,34−36,38] of NiO, Cr_2O_3, WO_3, etc. Mo^{VI}

Received: May 18, 2019
Revised: August 1, 2019
Published: August 9, 2019

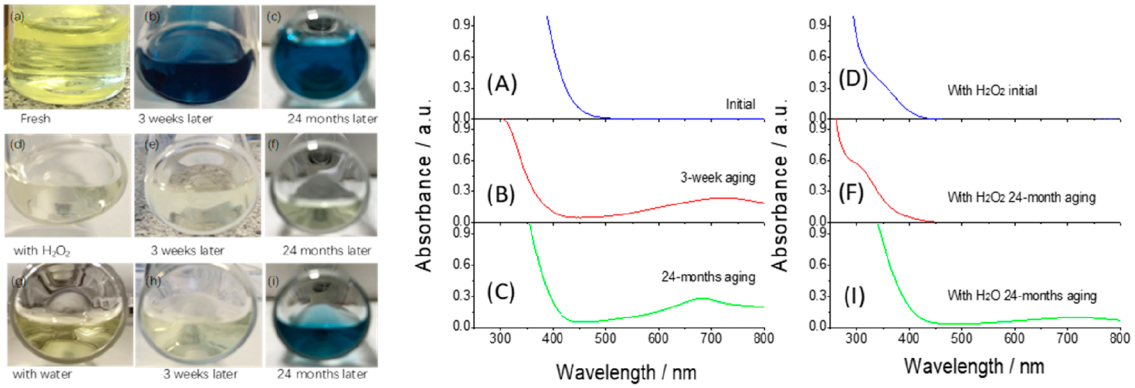

Figure 1. Digital images of the suspension of (a, b, c) the pristine sample, as well as those of (d, e, f) the H_2O_2-treated suspension and (g, h, i) the H_2O-treated suspension after anodization for different aging times. Light absorbance of the presentative samples in panels (a), (b), (c), (d), (f), and (i) are shown in panels (A), (B), (C), (D), (F), and (I), respectively.

oxide in the highest oxidation state shows different crystalline phases, depending on the synthetic routes:[39−41] four metastable phases have been reported for MoO_3 at high temperature or high pressure, in addition to the stable orthorhombic two-dimensional (2-D) α-MoO_3 phase.[42,43] For example, hexagonal molybdenum trioxide, which is a metastable phase that transforms to α-MoO_3 above 425 °C, has been reported to have a formula ranging from MoO_3 to $MoO_3{\cdot}nH_2O$ ($0.09 \leq n \leq 0.69$) and allows a versatile intercalation chemistry with interesting chemical, electrochemical, and catalytic properties.[40,44,45] The systematic study of the phase evolution of MoO_3 under different moisture and reducing/oxidation conditions would benefit the design and understanding of humidity sensing.

In this study, we employed microplasma-assisted anodization of molybdenum metal to synthesize MoO_3 nanocrystals, and the evolution of Mo species in anhydrous ethanol is examined over a period of two years to study the reduction and crystallization process. The anodization of Mo metal initially produces soluble Mo-oxyethoxide, accompanied by a small fraction of Mo oxide crystals. These nanoparticles with diameters of <10 nm are composed of hexagonal nanocrystals with an orthorhombic domain structure on the edge. The soluble species are subjected to reduction for the production of blue polyoxometalates (POMs) after an extended duration of aging at room temperature. The reducing agent for the POM clusters is the ethanol solvent being converted to ketones, but the addition of H_2O_2 to the initial suspension causes the formation of a dendritic porous framework containing hexagonal crystallites. The direct anodization of molybdenum under ionic-salt-free conditions provides an exemplar situation for studying the evolution of Mo species in both solid and liquid phases under adjustable water content, advancing the understanding of inherent chemical steps during the synthesis of Mo-based functional materials for sensing the humidity and reducing/oxidizing species. The solid product from the suspension is also demonstrated to be steadily responsive to relative humidity (RH) in the range of 11%−95%.

EXPERIMENTAL SECTION

Preparation of the Suspension. A cultivation basin containing 20 mL of absolute ethanol was used as the electrolytic tank and a graphite rod or a molybdenum bar was used as an anode (see Figure S1 in the Supporting Information). The depth of the Mo electrode was adjusted to give an immersed area of 5 cm^2. Helium gas passing through a nickel capillary was employed as the carrier gas of the microplasma for the cathode. The nickel capillary had inner and outer diameters of 0.7 and 1.0 mm, respectively, and the flow rate of helium was 50 standard cubic centimeters per minute (sccm). The microplasma at the gas/solution interface initiated under a DC bias of 3 kV was stabilized by a ballast resistor of 100 kΩ. The anodization process at a constant current of 6.1 mA lasted over 40 min for the production of the suspension.

Characterization of the Suspension. ^{1}H nuclear magnetic resonance (^{1}H NMR) of the suspension/solution in $CDCl_3$ before and after the anodization process was recorded at 300.06 MHz (Model Avance 300, Bruker, USA). The chemical shift of tetramethylsilane (TMS) was calibrated to be zero. An ultraviolet−visible light (UV−vis) absorption spectroscopy analysis of the suspension was recorded on a PerkinElmer Lambda 35 spectrometer that was equipped with an integrating sphere 150 mm in diameter. Transmission electron microscopy (TEM) images and selective area electron diffraction (SAED) patterns were obtained using a field-emission electron microscopy (FESEM) system (Model JEM-2100F, JEOL, Japan) coupled with energy-dispersive spectroscopy (EDS). The accelerating voltage for the electron beam of TEM was adjusted to be 200 keV. A coating on glass or silicon single crystal was obtained by dripping 100 μL of the anodized solution onto the substrate, followed by 5 h of drying in ambient air. The coatings were dried further at 60 °C for 1 h or 250 °C for 30 min, and then their superficial morphology is studied using scanning electron microscopy (SEM) (Model 6700F, JEOL, Japan).

Characterization of the Solid Products. X-ray photoemission spectroscopy (XPS) of the dried coatings was performed on a Kratos Axis Ultra XPS system that was equipped with a monochromatic X-ray source with an Al cathode ($K\alpha$ = 1468 eV). High-resolution core-level scans of Mo 3d, O 1s, C 1s, and the valence band were recorded at a resolution of 0.05 eV. The recorded XPS data were calibrated by fixing the C 1s to be 284.5 eV. A Kelvin probe from KPtechnology was used to measure the Fermi level of the coatings on silicon, and the values were calibrated against a gold reference. Powders of the solid product via the scratching of the dried coating were used for the Fourier transform infrared (FTIR) spectroscopy and thermogravimetric analysis (TGA). The FTIR analysis was performed on a spectrometer (Thermoscientific Nicolet iS5) with an attenuated total reflection (ATR) accessory. TGA, along with the simultaneous differential scanning calorimetry (DSC), in flowing synthetic air up to 800 °C was performed (Model SDT Q600, TA Instruments, USA).

Humidity Sensing. For the humidity sensors, 1 μL of suspension in ethanol was concentrated by drying in ambient air and dripping onto an interdigital electrode with a gold coating. Multiple drippings followed by drying at 60 °C were used to increase the thickness of the coating. The width of the gold coating (Figure S2 in the Supporting Information) and the blank space is 0.1 mm. Since different saturated salt solutions yield different relative humidity (RH) levels, saturated solutions of LiCl (11% RH), $MgCl_2$ (33% RH), $Mg(NO_3)_2$ (53% RH), NaCl (75% RH), KCl (85% RH), and KNO_3 (95% RH) were used to control the RH.[24,33] The measurements were performed by putting the

DOI: 10.1021/acs.cgd.9b00646
Cryst. Growth Des. 2019, 19, 5249−5257

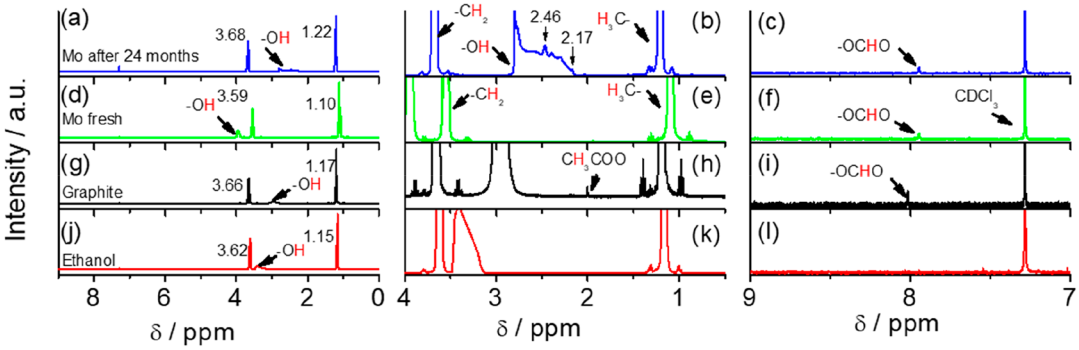

Figure 2. ^{1}H NMR of suspension in $CDCl_3$ after the anodization with graphite cathode and Mo^0 anode. The limiting currents for Mo and graphite anode are 6.1 and 4.6 mA, respectively. The spectrum of pure ethanol was provided for comparison, and the central position of the chemical shifts for the proton in $-CH_3$ and $-CH_2$ was indicated in panel (a). The NMR spectra for suspension with Mo (panels (d), (e), and (f)) and graphite (panels (g), (h), and (i)) are presented at different scales. Similarly, the spectra for pure ethanol (pannels (j), (k), and (l)) and the aged Mo suspension after 24 months (panels (a), (b), and (c)) are shown for comparison.

samples into the columns with different RH levels, while the direct-current (DC) conductivity was measured and recorded continuously using an electrochemical workstation (Zahner Pro, Zahner, Germany) at 18 °C.

RESULTS AND DISCUSSIONS

In the hybrid plasma-liquid systems, the auxiliary noble-metal electrode that is normally used in a standard electrochemical cell is replaced by a gas-plasma electrode, and this overcomes the issue of dissolution of the noble metal at high overpotential, which is the cause of increased costs and sample contamination.[46] Hot electrons, UV photons and a localized higher temperature interface produced in the plasma process induce the production of radicals in solution for prolonged times that affect the production of crystals afterward.[47] The soluble anodic product of the Mo^0 is Mo^{VI} in the form of molybdate or molybdic acid, depending on the pH of the solution, because the oxide film of lower valence could be a protective film on the surface.[16,48,49] Direct current anodization of Mo using LiCl electrolyte in ethanol under a bias above 110 V in a drybox produced a red brown product of molybdenum oxyethoxide.[50] In our case, after the anodization of Mo with microplasma as a counter electrode for 40 min, the absolute ethanol changed to a solution of yellowish color (Figure 1a) with an absorption edge of ~450 nm (Figure 1A). However, a dramatic color change was observed 3 weeks later for the samples that were encapsulated in a vial (Figure 1b); this blue solution can last for more than 2 years as long as good sealing of the vial is preserved (Figure 1c). The variation of color after the first 3 weeks is unnoticeable in a short period of time. The absorbance of the blue solution after 3 weeks of aging showed a broad peak at 721 nm, in addition to an absorption band with an edge at 400 nm in the blue side of the spectrum, which is a clear indication of Molybdenum Blue.[51] The formation of the blue species is dependent on the pH of the solution:[40] the solution should be acidic before and after the aging process.[51] After 2 years of aging in a sealed vial, the broad absorption that peaked at 721 nm in the sample after 3 weeks of aging shifted its peak to 686 nm, which is linked to the acidification of the solution that causes further reduction of Mo^{VI} cations.[52] Since the blue color is known to be from a lone pair of electrons as in Mo^{V},[53] 5 vol % H_2O_2 and H_2O were added to the yellowish solution (i.e., fresh samples) to explore the effect of electron acceptor and water content on the coloration of the solution. The addition of H_2O_2 changed instantly the original yellowish solution to a clear one (Figure 1d) and no blue product was found for the encapsulated solution in extended times (see Figures 1e and 1f). The solution with H_2O_2 showed a blue-shifted absorption edge (Figure 1D), with respect to the fresh one (Figure 1A), and did not exhibit any broad absorption in the longer wavelength region. H_2O_2 is not only an oxidizing agent that could be used to oxidize $MoO_{3-\delta}$ (δ is the oxygen deficiency) in aqueous solution under ambient conditions[54] but it is also a source of moisture for the solution; thus, H_2O was also added to a yellowish-colored fresh sample for comparison. The yellow tinge of the solution does not disappear instantly (Figure 1g) as in the case of H_2O_2, and no blue color was found after 3 weeks of aging, as evidenced in the image of Figure 1h. However, a light blue product (Figure 1i) was finally observed after 24 months of aging and the absorption spectrum showed the broad absorption peaking at 711 nm, indicating that the addition of moisture does not prohibit the reduction of Mo^{VI} species.[55] Zhang et al. prepared the blue POM using aqueous solution from a molybdate with ascorbic acid as a reducing agent and NaH_2PO_4 for the acidity,[52] so it is reasonable to conclude that H_2O is not able to oxidize the Mo^{V}-containing species during the plasma process, but it does affect the formation process of molybdenum blue (MB).

^{1}H NMR spectra revealed that the samples had no observable singlet peak at a chemical shift of 1.56 ppm for free water molecules in a $CDCl_3$ solvent[56] (Figure 2). The anhydrous condition promotes the formation of ethyl acetate from ethanol with the graphite electrode (Figure 2h), while acetic acid is produced with Co anode under a high voltage.[6] In the case of Mo anode, a trace amount of acetic acid is observed from NMR (see Figure S3 in the Supporting Information) for fresh and aged solutions, because molybdate is able to oxidize aldehyde into carboxylic acid.[57] Moreover, similar to the one with graphite anode (Figure 2i), formic acid was also found in the Mo-containing solution (see Figures 2c and 2f), indicating that the process can break the C−C bonds, and, thus, the formation of $\cdot CH_3$ free radicals is possible. For the solutions with Mo species (Figures 2a and 2b), an obvious change of the chemical shift to the high field was observed for the protons in $-CH_3$ and $-CH_2$ groups, compared to the original absolute ethanol, which indicates that ethanol and Mo species are forming a complex bonding. The ^{1}H NMR of formic acid in the fresh anodized solution with a Mo anode (Figure 2a) showed lower chemical shift, by 0.08 ppm, than the one with graphite anode (Figure 2c), indicating that they could also be connected to the Mo^{VI} cation.

DOI: 10.1021/acs.cgd.9b00646
Cryst. Growth Des. 2019, 19, 5249−5257

After the aging in a sealed vial, the protons in $-CH_2-$ and $-CH_3$ in the blue solution (inset in Figure 1b) containing Mo^V showed a larger chemical shift (Figures 2a and 2b) than the yellowish solution (Figures 2d and 2e) or pure ethanol (Figures 2j and 2k), which could be explained by the lower electronegativity of Mo^V than Mo^{VI} causing a reduction of electron density around the protons. An enlarged image of the NMR in Figure 2b shows a set of peaks with chemical shifts of 2.46 and 2.17 ppm, which could be assigned to the formation of acetone and/or ethyl methyl ketone in the suspension.[56] Although a plasma is well-known to produce long-lived radicals and electrons, which could act as the reducing agents for the Mo^{VI} species, the reducing agent could also be the ethoxide ligand on Mo^{VI} via discoordination and formation of ketones for the reactions after 3 weeks.[53,57] Commercially available yellow bis(acetylacetonate)-dioxomolybdenum(VI) ($MoO_2(acac)_2$) is reported to gradually convert to MB in a cyclohexanol solvent as a reducing agent.[53] Therefore, a similar mechanism of reduction could be written briefly as[53] where Et denotes an ethyl group. H_2O would

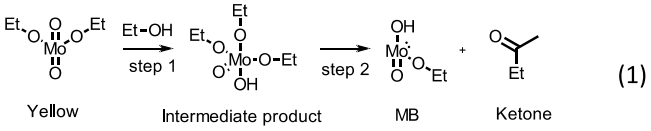

(1)

compete with EtOH to combine with the yellow intermediate product in step 1 or drive the reaction to the left side in step 2, thus retarding the formation of MB. Nonetheless, the addition of water did not prohibit the formation of MB as long as the sample is aged for a duration as long as 2 years.

When Mo is anodized in ethanol, some of the Mo species will be transported to ethanol to interact with the plasma cathode and liquid media. Solid particles were observed in the TEM analysis (Figure 3). Most of the particles are well-dispersed crystals with diameters of <10 nm (Figure 3a); a close-up image (Figure 3b) of the nanocrystals revealed that there are several domains. The nanoparticles are generally in hexagonal symmetry and the *d*-spacings are in agreement with hexagonal MoO_3, as shown in Figure 3b, although we are not clear about the actual water content in the lattice. The interaction of plasma and ambient air is known to reduce the pH of the solution, because of the formation of trace amoounts of NO_x and H_2O_2 that acidifies the solution.[58] The local anhydrous environment also causes the formation of α-MoO_3 on the edge of the particles, as shown in the higher-magnification images in Figures 3b and 3c. Note that the hexagonal and orthorhombic phase shares the crystal planes during the phase transition process and the *d*-spacings for (300) planes in the former is identical to that for the (200) plane in the latter.

Mo species in a reduced form can be also engineered in electron-rich POMs of different archetypes, structural flexibilities, and functionalities.[40,55] The valence reduction of Mo^{VI} in MoO_3 under a mild reduction environment in colloid systems can cause a color change and electronic structure variation under both solid and solution conditions.[51] The reduction of Mo^{VI} species by Mohr's salt, ethanol, formic acid, and $SnCl_2$ et al. can

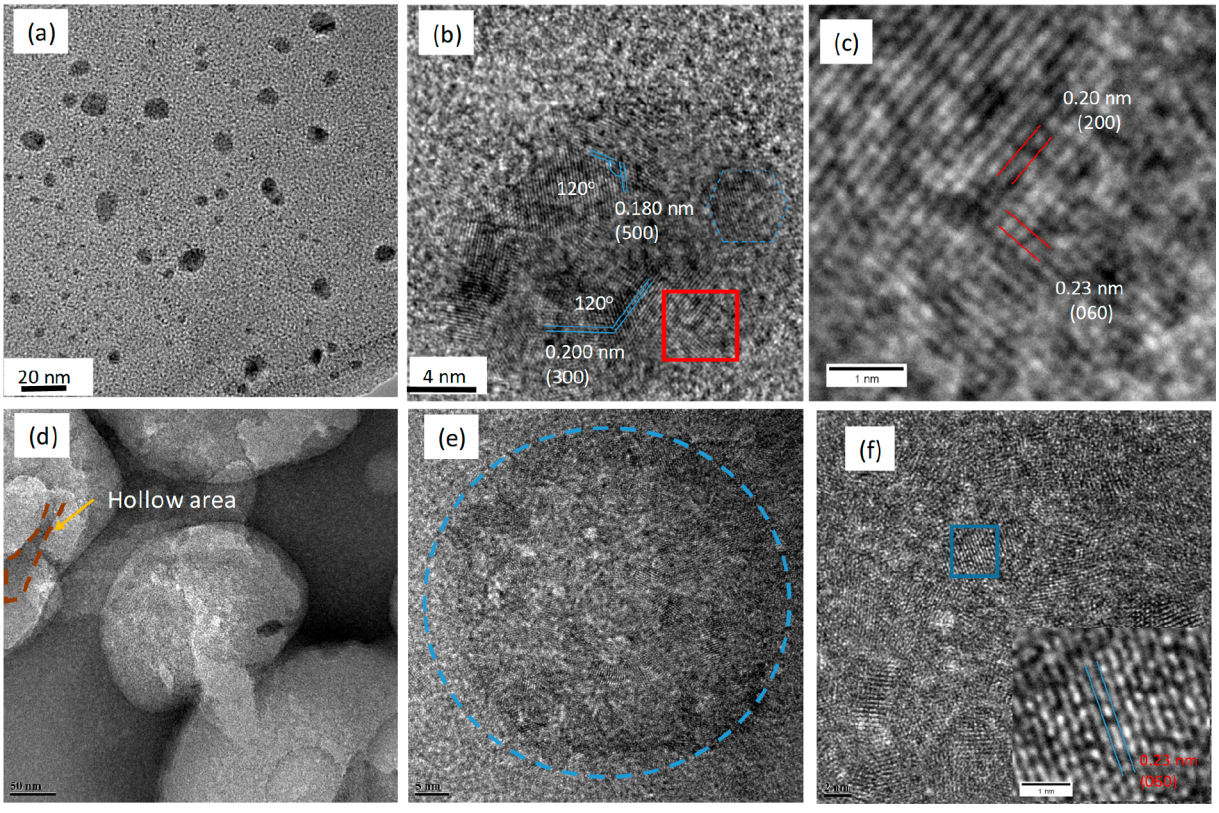

Figure 3. TEM images of the nanocrystals from the fresh (a, b, c) and aged blue suspension (d, e, f) under different magnifications. The *d*-spacings and angles in panel (b) belongs to hexagonal MoO_3. Panel (c) shows the higher-magnification image in the rectangle in panel (b). Panel (d) is the low-magnification view of the blue sample after 3 weeks of aging in capsulated vial, and anel (e) shows the effect of electron beam on the structure of particles. Panel (f) shows a higher-magnification image of the electron-beam annealed area. The inset in panel (f) shows the magnified image in the blue rectangle in panel (f).

DOI: 10.1021/acs.cgd.9b00646
Cryst. Growth Des. 2019, 19, 5249−5257

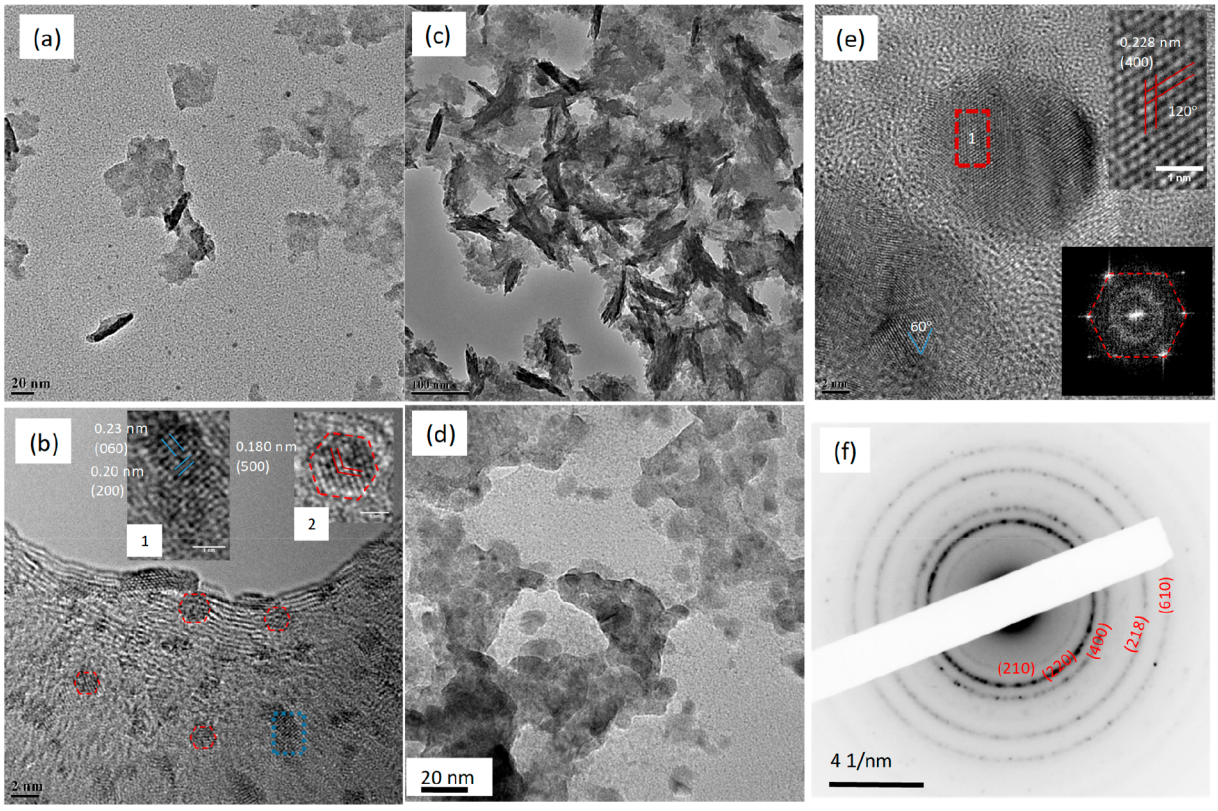

Figure 4. TEM images of the nanocrystals from (a, b) the fresh suspension and (c, d, e) the aged suspension with H_2O_2. Inset 1 in panel (b) shows the higher-magnification image in the blue rectangle, while inset 2 shows the magnified image in the red hexagon. Fast Fourier transform (FFT) transformation was performed on the round crystal at the center of the image shown in panel (e), and the magnified image in red rectangle is also shown as an inset as well. Panel (f) shows a slected-area electron diffraction (SAED) image of the materials shown in panel (d).

produce the well-known MB under acidic conditions containing giant POM clusters (on the scale of 1−100 nm) through the crystallization and precipitation process.[55] Reduced Mo species with lone-pair electrons on the Mo cation, showing brilliant colors, can absorb H_2O or other small molecules as ligands and can be used for the clinical agent or clock reactions, because of its special photothermal properties.[52,53] The TEM image of the blue sample (Figure 3d) showed that Mo species grew up to beads larger than 200 nm after 3 weeks. Some of the large clusters are hollow in the middle, as can be seen from the broken particles (Figure 3d) as a result of the electron-doping and linking ligand assisting the formation of amphiphilic O═MoL (where L = small molecular ligands),[51] which promoted the ring-shaped supramolecular clusters.[51] These giant clusters precipitated as the amount of Mo^V species exceeded its solubility in ethanol and formed suspended particles and the hollow structure is attractive, because of the special properties in many applications.[44] The detailed high-resolution imaging of the structure of the blue precipitate is very difficult, because it suffers structure change under the electron beam, which could be related to the evaporation of small molecules, such as ethanol, formic acid, etc., adsorbed in the giant structure. However, from the TEM image, we can determine that the intact beads showed that defective domains of α-MoO_3 can be determined after annealing under an electron beam (see Figures 3e and 3f). The formation of defective domains and structure change can be related to the loss of small molecule ligands under the electron beam.

The addition of H_2O_2 dramatically changed the morphology of the particles in the products. H_2O_2 caused the recrystallization of the Mo species, as can be seen from the sharp edges and crystal aggregation in the TEM image (see Figures 4a and 4b); EDS analysis (Figure S4 in the Supporting Information) verified that the Mo species are primarily contained. The fine crystalline particles are composed of both hexagonal and orthorhombic MoO_3 crystals (Figure 4b), but the two phases are less likely to form a montage of crystals. After 3 weeks of aging, the quantity of crystalline phases increased significantly and formed a dendritic framework, as shown in Figures 4c and 4d, and the detailed imaging of the single particles showed a hexagonal structure (Figure 4e). The detailed imaging and the corresponding SAED pattern (Figures 4d and 4f) showed that this framework was composed mostly of h-MoO_3 crystallite and on the scale of 20 nm in diameter. These observations indicate that the instant reaction between H_2O_2 and the Mo species are in the liquid phase after the addition of H_2O_2, since the reaction in solid state would require long distance diffusion of ions and extended times, but it will affect the production of Mo particles afterward.

Since the Mo species could form complexes with ethanol, water molecules, and other small molecules that were produced during plasma-assisted anodization, the weight of these ligands were analyzed using simultaneous thermogravimetric analysis (TGA) and differential scanning calorimetry (DSC) under an air atmosphere (Figure 5). The weight loss of the sample with a predrying in air at 80 °C loses 24% of its total weight up to 500 °C. The decomposition of 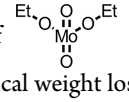 to MoO_3 would be expected to induce a theoretical weight loss of 34.5%, and lower

DOI: 10.1021/acs.cgd.9b00646
Cryst. Growth Des. 2019, 19, 5249−5257

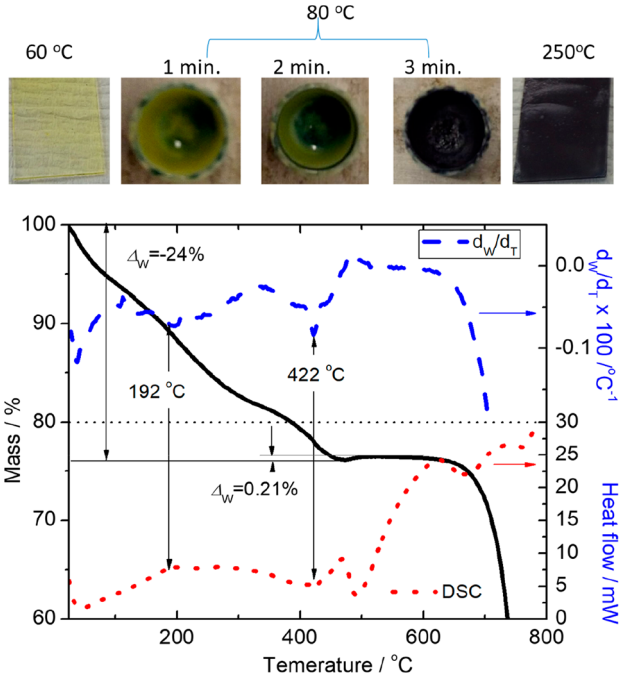

Figure 5. Simultaneous TGA and DSC curves in flowing air for the powders after the drying at 80 °C for 0.5 h in the ambient air. The images above the TGA curves show the color variation of the suspension/solid product at different temperatures and annealing times at 80 °C.

weight loss in our TGA could be explained by the initial prior weight loss that was incurred when the sample was dried at 80 °C. An obvious endothermic peak with a simultaneous derivative thermogravimetric peak was observed at 422 °C, which is very close to the phase transition temperature (425 °C (ref 40)) between the hexagonal to orthorhombic MoO_3.[59] The weight gain at 486 °C could be the oxygenation of the oxide after the fully decoordination of organic groups.[60] At temperatures of >650 °C, the oxides start to lose weight, because of the formation of oxygen vacancies.

Molybdenum oxides can be processed to dense coatings, dispersed nanoparticles/plates, or mesoporous frameworks for energy applications.[59,61−64] The kinetics for the formation of Mo^V species in the photothermal reaction is dependent on temperature and the concentration of Mo species in the solution.[53] The fresh suspension underwent color change very quickly at 80 °C and become dark brown after 3 min, as can be seen from the images in Figure 5. SEM analysis of the dark brown film formed at 80 °C on glass (Figure S5 in the Supporting Information) showed a dense surface, while the growth of first-order hierarchical structures can be achieved via the annealing of a mixture of ammonium molybdate and citrate acid as a meditator[65] or chemical vapor deposition (CVD).[66] The initial yellow film with a bandgap of 2.68 eV, as indicated in the Tauc plot in Figure S6 in the Supporting Information, becomes dark brown, showing high absorption even in the near-infrared (NIR) region after the calcination at 250 °C (see Figure S6). The strong absorption at 900 nm could be explained by the intermediate electronic state near the Fermi level, as in the X-ray photoemission spectroscopy (XPS) valence band (Figure 6), because of the formation of Mo^V and the oxygen vacancies,[67] since the conduction band of MoO_3 is dominated by Mo d states with some hybridization with O 2p states.[68] Mo^V accounts for 20% of the Mo cations after the calcination at 250 °C, by comparing the deconvoluted area for Mo^V and Mo^{VI} in the Mo 3d spectra. MoOx crystals were synthesized hydrothermally using H_2MoO_4 in the presence of polyethylene glycol (PEG) and found that the presence of 100 g/L PEG induces spherical crystals containing Mo^V and Mo^{IV}.[69] Although the product has not been converted fully to oxides at temperatures of <250 °C, the work function (Figure S7 in the Supporting Information) of the coating is in the range between −5.06 eV and −5.24 eV, which is close to that of the air-exposed MoO_3 (−5.3 eV).[70] As a typical *n*-type semiconductor, the Fermi level could be close to the minimum of conduction band and the rising of density of state near the Fermi level would not induce major change to the Fermi level. The FTIR spectrum (Figure S8 in the Supporting Information) of the fresh suspension dried at 60 °C showed clear absorption peaks for vibrations of Mo═O bonds (977 and 911 cm^{-1}) and Mo−O bonds (below 650 cm^{-1}),[13] but the one for oxygen stretching in Mo−O−Mo (860 cm^{-1}) was presented as a shoulder to the one at 911 cm^{-1}. This indicates that the product of anodization is molybdenum oxyethoxide, rather than pure ethoxide, after the anodization process. The presence of ethoxide anion could also explain the lower binding energy and smaller for the Mo^{VI} in molybdenum dried at 60 °C (denoted as Mo60) than in molybdenum dried at 250 °C (denoted as Mo250) because of the loss of ethoxide in the latter. After the thermal treatment at 250 °C, the peak at 911 cm^{-1} for the Mo═O bond disappeared but is replaced by a wide peak below 930 cm^{-1}, which could be ascribed to the vibration of the O atom linking multiple Mo atoms after the loss of organics and

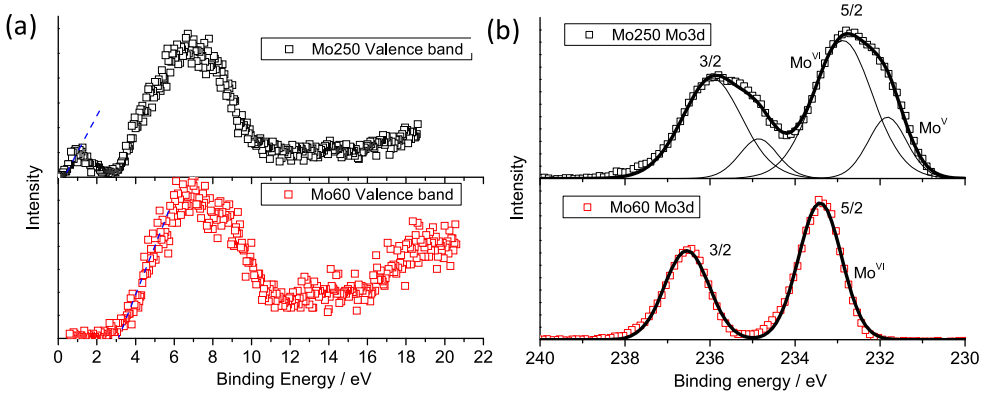

Figure 6. XPS of the coating after drying at 60 °C (denoted as Mo60) and 250 °C (denoted as Mo250): (a) valence band and (b) Mo 3d.

DOI: 10.1021/acs.cgd.9b00646
Cryst. Growth Des. 2019, 19, 5249−5257

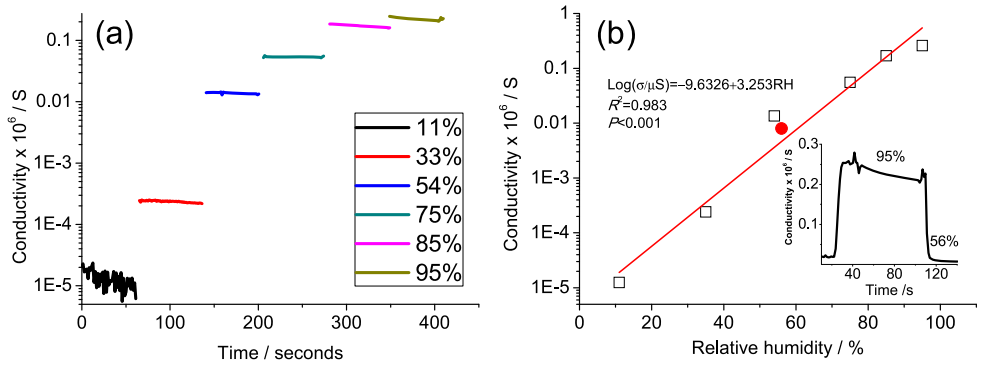

Figure 7. (a) Conductivity variation under different relative humidity (RH) values at 18 °C and (b) a plot of log(σ) versus RH. The red dot in panel (b) shows the resistivity and relative humidity in ambient air, and the inset depicts a typical response and recovery cycle.

the formation Mo−O−Mo bonds. More importantly, an obvious broad peak for the OH group at 3400 cm^{-1} was found in the sample dried at 60 °C, which clearly indicates the interaction between the water molecules and the MoO_3 oxides.

As can be seen from the aforementioned study, the structure of MoO_3 can be affected by thermal treatment and water molecules, so a thin-film interdigital electrode was employed to study the humidity sensing properties. The electric resistivity (σ) of the electrode is affected significantly by the variation of RH (Figure 7), and a linear plot can be achieved in the plot of humidity versus log(σ). The response time at 95% RH, for example, only requires 10 s, while the recovery times are <3 s, which is comparable to nanocrystalline CeO_2 asa humidity sensor[25] but is shorter than MoO_3 film from CVD technique (60 s to respond, 5 s to recover[33]). The increase of conductivity with humidity on ceramic sensors is attributed to the adsorption of water molecules on the defect site of the oxides,[23] generating a proton conductivity. In the suspension containing nanocrystals Mo^{VI} species, the absorbed water molecules can be dissociated to give an increased proton conductivity:

$$2H_2O = H_3O^+ + OH^- \quad (2)$$

The adsorption of water molecules can be evidenced by the FTIR analysis, and the result is consistent with the observation of hexagonal MoO_3 containing water molecules in the TEM analysis. Chithambararaj et al.[71] studied the electric properties of h-MoO_3 and α-MoO_3 and found that the former could show superionic conductance under the condition of water or ammonia molecules.

CONCLUSION

Molybdenum metal (Mo^0) was anodized in a pure ethanol electrolyte at high voltage with a gaseous microplasma electrode under ambient conditions. The product shortly after the synthesis process is mostly Mo oxyethoxide, which is soluble in ethanol solvent. However, small amounts of MoO_3 crystals containing mixed hexagonal and orthorhombic phases were produced and the (300) planes in the former share the (200) planes in the latter. Ethanol is the reducing agent for the transition between Mo^{VI} to Mo^V cation with lone-pair electrons and ethanol molecules can also be the small molecules absorbing on the Mo^V to form POMs. The oxidation of ethanol, in our case, produces ketone rather than aldehyde or carboxylate. In addition, water is critically important to the reduction kinetics of Mo^V while H_2O_2 is able to promote a dendritic framework of hexagonal MoO_3 crystallite. The light absorbance of the coating varies with the thermal treatment at 250 °C and midgap states evolved and this could increase the conductivity of the solids. The coating can be used for humidity sensing based on facile electrical conductivity measurement, because of the (de)-adsorption of water molecules affecting the protonic conduction at 18 °C. The study of crystal evolution of MoO_3 species under water, ethanol, and H_2O_2 would benefit the design and understanding of the sensing of different gases.

ASSOCIATED CONTENT

Supporting Information

The Supporting Information is available free of charge on the ACS Publications website at DOI: 10.1021/acs.cgd.9b00646.

Testing setup; geometry of interdigital electrode; ^{1}H NMR; workfunction by Kelvin probe; UV-vis light absorption of coatings; FTIR, SEM, and EDS results (PDF)

AUTHOR INFORMATION

Corresponding Author

*E-mail addresses: nichengsheg@swu.edu.cn, nichengsheg@163.com.

ORCID

Chengsheng Ni: 0000-0002-7184-1654
Darragh Carolan: 0000-0003-2200-6174
John Irvine: 0000-0002-8394-3359
Paul Maguire: 0000-0002-2725-4647
Davide Mariotti: 0000-0003-1504-4383

Notes

The authors declare no competing financial interest.
Dataset related to this publication can be found at https://www.doi.org/10.21251/e68b2fef-5e72-41fe-b93e-7295422c138a.

ACKNOWLEDGMENTS

We would like to thank the support from National Natural Science Foundation of China (NSFC) (Nos. 51702264 and 41371275), Fundamental Research Funds for the Central Universities (No. XDJK2017B033), and Research Funding of Southwest University (No. SWU117019). The funding from the Engineering and Physical Sciences Research Council (EPSRC) (under Grant Nos. EP/K022237/1, EP/K036769/1, and EP/M024938/1) is also acknowledged. We also appreciate the funding from the EU COST Action (No. TD1208) for useful exchanges and discussions. We also thank Ms. Zhang Ziye (Southwest University) for the measurement of conductivity under different relative humidity values.

DOI: 10.1021/acs.cgd.9b00646
Cryst. Growth Des. 2019, 19, 5249−5257

REFERENCES

(1) Pinna, N.; Niederberger, M. Surfactant-Free Nonaqueous Synthesis of Metal Oxide Nanostructures. *Angew. Chem., Int. Ed.* **2008**, *47*, 5292−5304.

(2) Cheng, F.; Shen, J.; Peng, B.; Pan, Y.; Tao, Z.; Chen, J. Rapid room-temperature synthesis of nanocrystalline spinels as oxygen reduction and evolution electrocatalysts. *Nat. Chem.* **2011**, *3*, 79−84.

(3) Welton, T. Room-Temperature Ionic Liquids. Solvents for Synthesis and Catalysis. *Chem. Rev. (Washington, DC, U. S.)* **1999**, *99*, 2071−2084.

(4) Maguire, P.; Rutherford, D.; Macias-Montero, M.; Mahony, C.; Kelsey, C.; Tweedie, M.; Pérez-Martin, F.; McQuaid, H.; Diver, D.; Mariotti, D. Continuous In-Flight Synthesis for On-Demand Delivery of Ligand-Free Colloidal Gold Nanoparticles. *Nano Lett.* **2017**, *17*, 1336−1343.

(5) Wang, R.; Zuo, S.; Wu, D.; Zhang, J.; Zhu, W.; Becker, K. H.; Fang, J. Microplasma-Assisted Synthesis of Colloidal Gold Nanoparticles and Their Use in the Detection of Cardiac Troponin I (cTn-I). *Plasma Processes Polym.* **2015**, *12*, 380−391.

(6) Ni, C.; Carolan, D.; Rocks, C.; Hui, J.; Fang, Z.; Padmanaban, D. B.; Ni, J.; Xie, D.; Maguire, P.; Irvine, J. T. S.; Mariotti, D. Microplasma-assisted electrochemical synthesis of Co_3O_4 nanoparticles in absolute ethanol for energy applications. *Green Chem.* **2018**, *20*, 2101−2109.

(7) Velusamy, T.; Liguori, A.; Macias-Montero, M.; Padmanaban, D. B.; Carolan, D.; Gherardi, M.; Colombo, V.; Maguire, P.; Svrcek, V.; Mariotti, D. Ultra-small CuO nanoparticles with tailored energy-band diagram synthesized by a hybrid plasma-liquid process. *Plasma Processes Polym.* **2017**, *14*, 1600224.

(8) Du, C.; Xiao, M. Cu_2O nanoparticles synthesis by microplasma. *Sci. Rep.* **2015**, *4*, 7339.

(9) Senthilnathan, J.; Weng, C.-C.; Liao, J.-D.; Yoshimura, M. Submerged Liquid Plasma for the Synthesis of Unconventional Nitrogen Polymers. *Sci. Rep.* **2013**, *3*, 2414.

(10) Carolan, D.; Rocks, C.; Padmanaban, D. B.; Maguire, P.; Svrcek, V.; Mariotti, D. Environmentally friendly nitrogen-doped carbon quantum dots for next generation solar cells. *Sustainable Energy Fuels* **2017**, *1*, 1611−1619.

(11) Stubhan, T.; Ameri, T.; Salinas, M.; Krantz, J.; Machui, F.; Halik, M.; Brabec, C. J. High shunt resistance in polymer solar cells comprising a MoO_3 hole extraction layer processed from nanoparticle suspension. *Appl. Phys. Lett.* **2011**, *98*, 253308.

(12) Lou, X. W.; Zeng, H. C. Complex alpha-MoO_3 nanostructures with external bonding capacity for self-assembly. *J. Am. Chem. Soc.* **2003**, *125*, 2697−2704.

(13) Wongkrua, P.; Thongtem, T.; Thongtem, S. Synthesis of h- and alpha-MoO_3 by Refluxing and Calcination Combination: Phase and Morphology Transformation, Photocatalysis, and Photosensitization. *J. Nanomater.* **2013**, *2013*, 1.

(14) Knorr, K.; Leslie, J. D. Plasma anodization of titanium and molybdenum. *Thin Solid Films* **1974**, *23*, 101−107.

(15) Ikonopisov, S. Electrolytes for anodization of molybdenum. *Electrodeposition Surf. Treat.* **1974**, *2*, 411−418.

(16) Badawy, W. A.; Gad-Allah, A. G.; Abd El-Rahman, H. A.; Abou-Romia, M. M. On the stability of anodic oxide films formed on molybdenum in various aqueous solutions. *Surf. Coat. Technol.* **1987**, *30*, 365−373.

(17) Yao, D. D.; Ou, J. Z.; Latham, K.; Zhuiykov, S.; O'Mullane, A. P.; Kalantar-Zadeh, K. Electrodeposited alpha- and beta-Phase MoO_3 Films and Investigation of Their Gasochromic Properties. *Cryst. Growth Des.* **2012**, *12*, 1865−1870.

(18) Chen, Q.; Kitamura, T.; Saito, K.; Haruta, K.; Yamano, Y.; Ishikawa, T.; Shirai, H. Microplasma discharge in ethanol solution: Characterization and its application to the synthesis of carbon microstructures. *Thin Solid Films* **2008**, *516*, 4435−4440.

(19) Lv, C.; Hu, C.; Luo, J.; Liu, S.; Qiao, Y.; Zhang, Z.; Song, J.; Shi, Y.; Cai, J.; Watanabe, A. Recent Advances in Graphene-Based Humidity Sensors. *Nanomaterials* **2019**, *9*, 422.

(20) Kuang, Q.; Lao, C.; Wang, Z. L.; Xie, Z.; Zheng, L. High-Sensitivity Humidity Sensor Based on a Single SnO_2 Nanowire. *J. Am. Chem. Soc.* **2007**, *129*, 6070−6071.

(21) Lu, T.; Song, H. J.; Dong, X. Q.; Hu, J. Y.; Lv, Y. A highly selective and fast-response photoluminescence humidity sensor based on F-decorated NH2-MIL-53(Al) nanorods. *J. Mater. Chem. C* **2017**, *5*, 9465−9471.

(22) Shimizu, Y.; Shimabukuro, M.; Arai, H.; Seiyama, T. Humidity-Sensitive Characteristics of La^{3+}-Doped and Undoped $SrSnO_3$. *J. Electrochem. Soc.* **1989**, *136*, 1206−1210.

(23) Traversa, E. Ceramic sensors for humidity detection: the state-of-the-art and future developments. *Sens. Actuators, B* **1995**, *23*, 135−156.

(24) Li, M.; Chen, X. L.; Zhang, D. F.; Wang, W. Y.; Wang, W. J. Humidity sensitive properties of pure and Mg-doped $CaCu_3Ti_4O_{12}$. *Sens. Actuators, B* **2010**, *147*, 447−452.

(25) Xie, W.; Liu, B.; Xiao, S.; Li, H.; Wang, Y.; Cai, D.; Wang, D.; Wang, L.; Liu, Y.; Li, Q.; Wang, T. High performance humidity sensors based on CeO_2 nanoparticles. *Sens. Actuators, B* **2015**, *215*, 125−132.

(26) Yang, S.; Liu, Y.; Chen, W.; Jin, W.; Zhou, J.; Zhang, H.; Zakharova, G. S. High sensitivity and good selectivity of ultralong MoO_3 nanobelts for trimethylamine gas. *Sens. Actuators, B* **2016**, *226*, 478−485.

(27) Pandeeswari, R.; Jeyaprakash, B. G. Nanostructured alpha-MoO_3 thin film as a highly selective TMA sensor. *Biosens. Bioelectron.* **2014**, *53*, 182−186.

(28) Guentner, A. T.; Righettoni, M.; Pratsinis, S. E. Selective sensing of NH_3 by Si-doped alpha-MoO3 for breath analysis. *Sens. Actuators, B* **2016**, *223*, 266−273.

(29) Wang, L.; Gao, P.; Bao, D.; Wang, Y.; Chen, Y.; Chang, C.; Li, G.; Yang, P. Synthesis of Crystalline/Amorphous Core/Shell MoO_3 Composites through a Controlled Dehydration Route and Their Enhanced Ethanol Sensing Properties. *Cryst. Growth Des.* **2014**, *14*, 569−575.

(30) Munasinghe Arachchige, H.; Zappa, D.; Poli, N.; Gunawardhana, N.; Comini, E. Gold functionalized MoO3 nano flakes for gas sensing applications. *Sens. Actuators, B* **2018**, *269*, 331−339.

(31) Illyaskutty, N.; Kohler, H.; Trautmann, T.; Schwotzer, M.; Mahadevan Pillai, V. P. Hydrogen and ethanol sensing properties of molybdenum oxide nanorods based thin films: Effect of electrode metallization and humid ambience. *Sens. Actuators, B* **2013**, *187*, 611−621.

(32) Li, D.; Li, Y.; Li, F.; Zhang, J.; Zhu, X.; Wen, S.; Ruan, S. Humidity sensing properties of MoO_3-NiO nanocomposite materials. *Ceram. Int.* **2015**, *41*, 4348−4353.

(33) Jadkar, V.; Pawbake, A.; Waykar, R.; Jadhavar, A.; Mayabadi, A.; Date, A.; Late, D.; Pathan, H.; Gosavi, S.; Jadkar, S. Synthesis of orthorhombic-molybdenum trioxide (alpha-MoO_3) thin films by hot wire-CVD and investigations of its humidity sensing properties. *J. Mater. Sci.: Mater. Electron.* **2017**, *28*, 15790−15796.

(34) Kim, H.-U.; Son, J.; Kulkarni, A.; Ahn, C.; Kim, K. S.; Shin, D.; Yeom, G. Y.; Kim, T. Highly uniform wafer-scale synthesis of alpha-MoO_3 by plasma enhanced chemical vapor deposition. *Nanotechnology* **2017**, *28*, 175601.

(35) Pokhrel, S.; Nagaraja, K. S. Solid state electrical conductivity and humidity sensing properties of Cr_2O_3-MoO_3 composites. *Physica Status Solidi a-Applications and Materials Science* **2002**, *194*, 140−146.

(36) Pokhrel, S.; Nagaraja, K. S. Electrical and humidity sensing properties of molybdenum(VI) oxide and tungsten(VI) oxide composites. *Physica Status Solidi a-Applied Research* **2003**, *198*, 343−349.

(37) Babu Reddy, L. P.; Megha, R.; Chethan, B.; Raj Prakash, H. G.; Ravikiran, Y. T.; Ramana, C. H. V. V.; Kim, D. Role of molybdenum trioxide in enhancing the humidity sensing performance of magnesium ferrite/molybdenum trioxide composite. *Inorg. Chem. Commun.* **2018**, *98*, 68−74.

(38) Sundaram, R.; Nagaraja, K. S. Solid state electrical conductivity and humidity sensing studies on metal molybdate-molybdenum trioxide composites (M = Ni^{2+} Cu^{2+} and Pb^{2+}). *Sens. Actuators, B* **2004**, *101*, 353−360.

DOI: 10.1021/acs.cgd.9b00646
Cryst. Growth Des. 2019, 19, 5249−5257

(39) Lunk, H.-J.; Hartl, H.; Hartl, M. A.; Fait, M. J. G.; Shenderovich, I. G.; Feist, M.; Frisk, T. A.; Daemen, L. L.; Mauder, D.; Eckelt, R.; Gurinov, A. A. Hexagonal Molybdenum Trioxide"—Known for 100 Years and Still a Fount of New Discoveries. *Inorg. Chem.* **2010**, *49*, 9400−9408.
(40) Zheng, L.; Xu, Y.; Jin, D.; Xie, Y. Novel Metastable Hexagonal MoO3 Nanobelts: Synthesis, Photochromic, and Electrochromic Properties. *Chem. Mater.* **2009**, *21*, 5681−5690.
(41) Sakaushi, K.; Thomas, J.; Kaskel, S.; Eckert, J. Aqueous Solution Process for the Synthesis and Assembly of Nanostructured One-Dimensional alpha-MoO_3 Electrode Materials. *Chem. Mater.* **2013**, *25*, 2557−2563.
(42) Hu, X. K.; Qian, Y. T.; Song, Z. T.; Huang, J. R.; Cao, R.; Xiao, J. Q. Comparative study on MoO_3 and H_xMoO_3 nanobelts: Structure and electric transport. *Chem. Mater.* **2008**, *20*, 1527−1533.
(43) Ren, H.; Sun, S.; Cui, J.; Li, X. Synthesis, Functional Modifications, and Diversified Applications of Molybdenum Oxides Micro-/Nanocrystals: A Review. *Cryst. Growth Des.* **2018**, *18*, 6326−6369.
(44) Mariotti, D.; Lindström, H.; Bose, A. C.; Ostrikov, K. K. Monoclinic β-MoO_3 nanosheets produced by atmospheric microplasma: application to lithium-ion batteries. *Nanotechnology* **2008**, *19*, 495302.
(45) Kiebach, R.; Pienack, N.; Bensch, W.; Grunwaldt, J. D.; Michailovski, A.; Baiker, A.; Fox, T.; Zhou, Y.; Patzke, G. R. Hydrothermal formation of W/Mo-Oxides: A multidisciplinary study of growth and shape. *Chem. Mater.* **2008**, *20*, 3022−3033.
(46) Richmonds, C.; Witzke, M.; Bartling, B.; Lee, S. W.; Wainright, J.; Liu, C.-C.; Sankaran, R. M. Electron-Transfer Reactions at the Plasma-Liquid Interface. *J. Am. Chem. Soc.* **2011**, *133*, 17582−17585.
(47) Mariotti, D.; Švrček, V.; Hamilton, J. W. J.; Schmidt, M.; Kondo, M. Silicon Nanocrystals in Liquid Media: Optical Properties and Surface Stabilization by Microplasma-Induced Non-Equilibrium Liquid Chemistry. *Adv. Funct. Mater.* **2012**, *22*, 954−964.
(48) Mahadevaiah, N.; Venkataramani, B.; Jai Prakash, B. S. Restrictive entry of aqueous molybdate species into surfactant modified montmorillonite - A breakthrough curve study. *Chem. Mater.* **2007**, *19*, 4606−4612.
(49) Pereira, A. C.; Ferreira, T. L.; Kosminsky, L.; Matos, R. C.; Bertotti, M.; Tabacniks, M. H.; Kiyohara, P. K.; Fantini, M. C. A. Characterization of electrochemically co-deposited metal-molybdenum oxide films. *Chem. Mater.* **2004**, *16*, 2662−2668.
(50) Kessler, V. G.; Panov, A. N.; Turova, N. Y.; Starikova, Z. A.; Yanovsky, A. I.; Dolgushin, F. M.; Pisarevsky, A. P.; Struchkov, Y. T. Anodic oxidation of molybdenum and tungsten in alcohols: isolation and X-ray single-crystal study of side products. *J. Chem. Soc., Dalton Trans.* **1998**, 21−30.
(51) Müller, A.; Serain, C. Soluble Molybdenum Blues"des Pudels Kern. *Acc. Chem. Res.* **2000**, *33*, 2−10.
(52) Zhang, C.; Bu, W. B.; Ni, D. L.; Zuo, C. J.; Cheng, C.; Li, Q.; Zhang, L. L.; Wang, Z.; Shi, J. L. A Polyoxometalate Cluster Paradigm with Self-Adaptive Electronic Structure for Acidity/Reducibility-Specific Photothermal Conversion. *J. Am. Chem. Soc.* **2016**, *138*, 8156−8164.
(53) Neuenschwander, U.; Negron, A.; Jensen, K. F. A Clock Reaction Based on Molybdenum Blue. *J. Phys. Chem. A* **2013**, *117*, 4343−4351.
(54) Sharma, A. K.; Pandey, S.; Sharma, K. H.; Nerthigan, Y.; Khan, M. S.; Hang, D. R.; Wu, H. F. Two dimensional alpha-MoO3-x nanoflakes as bare eye probe for hydrogen peroxide in biological fluids. *Anal. Chim. Acta* **2018**, *1015*, 58−65.
(55) Gumerova, N. I.; Rompel, A. Synthesis, structures and applications of electron-rich polyoxometalates. *Nat. Rev. Chem.* **2018**, *2*, DOI: 10.1038/s41570-018-0112.
(56) Gottlieb, H. E.; Kotlyar, V.; Nudelman, A. NMR chemical shifts of common laboratory solvents as trace impurities. *J. Org. Chem.* **1997**, *62*, 7512−7515.
(57) Trost, B. M.; Masuyama, Y. Chemoselectivity in molybdenum catalyzed alcohol and aldehyde oxidations. *Tetrahedron Lett.* **1984**, *25*, 173−176.
(58) Rumbach, P.; Witzke, M.; Sankaran, R. M.; Go, D. B. Decoupling Interfacial Reactions between Plasmas and Liquids: Charge Transfer vs Plasma Neutral Reactions. *J. Am. Chem. Soc.* **2013**, *135*, 16264−16267.
(59) Epifani, M.; Imperatori, P.; Mirenghi, L.; Schioppa, M.; Siciliano, P. Synthesis and characterization of MoO_3 thin films and powders from a molybdenum chloromethoxide. *Chem. Mater.* **2004**, *16*, 5495−5501.
(60) Lu, X.; Wang, R.; Yang, F.; Jiao, W.; Liu, W.; Hao, L.; He, X. Preparation of MoO_3 QDs through combining intercalation and thermal exfoliation. *J. Mater. Chem. C* **2016**, *4*, 6720−6726.
(61) Nanayakkara, C. E.; Vega, A.; Liu, G.; Dezelah, C. L.; Kanjolia, R. K.; Chabal, Y. J. Role of Initial Precursor Chemisorption on Incubation Delay for Molybdenum Oxide Atomic Layer Deposition. *Chem. Mater.* **2016**, *28*, 8591−8597.
(62) Wang, G.; Ji, Y.; Zhang, L. H.; Zhu, Y. M.; Gouma, P. I.; Dudley, M. Synthesis of molybdenum oxide nanoplatelets during crystallization of the precursor gel from its hybrid nanocomposites. *Chem. Mater.* **2007**, *19*, 979−981.
(63) Shukoor, M. I.; Therese, H. A.; Gorgishvili, L.; Glasser, G.; Kolb, U.; Tremel, W. From layered molybdic acid to lower-dimensional nanostructures by intercalation of amines under ambient conditions. *Chem. Mater.* **2006**, *18*, 2144−2151.
(64) Hosono, K.; Matsubara, I.; Murayama, N.; Woosuck, S.; Izu, N. Synthesis of polypyrrole/MoO_3 hybrid thin films and their volatile organic compound gas-sensing properties. *Chem. Mater.* **2005**, *17*, 349−354.
(65) Cong, S.; Sugahara, T.; Wei, T.; Jiu, J.; Hirose, Y.; Nagao, S.; Suganuma, K. Growth and Extension of One-Step Sol-Gel Derived Molybdenum Trioxide Nanorods via Controlling Citric Acid Decomposition Rate. *Cryst. Growth Des.* **2015**, *15*, 4536−4542.
(66) Badica, P. Preparation through the vapor transport and growth mechanism of the first-order hierarchical structures of MoO_3 belts on sillimanite fibers. *Cryst. Growth Des.* **2007**, *7*, 794−801.
(67) Akande, S. O.; Chroneos, A.; Vasilopoulou, M.; Kennou, S.; Schwingenschlögl, U. Vacancy formation in MoO_3: hybrid density functional theory and photoemission experiments. *J. Mater. Chem. C* **2016**, *4*, 9526−9531.
(68) Scanlon, D. O.; Watson, G. W.; Payne, D. J.; Atkinson, G. R.; Egdell, R. G.; Law, D. S. L. Theoretical and Experimental Study of the Electronic Structures of MoO_3 and MoO_2. *J. Phys. Chem. C* **2010**, *114*, 4636−4645.
(69) Li, X.-y.; Xiao, Q.-g.; Ning, P.-g.; Xu, H.-b.; Zhang, Y. Morphological and Structural Diversity of Molybdenum Oxide-Based Hybrid Materials Prepared through PEG Induction. *Cryst. Growth Des.* **2016**, *16*, 1512−1518.
(70) Irfan; Ding, H.; Gao, Y.; Small, C.; Kim, D. Y.; Subbiah, J.; So, F. Energy level evolution of air and oxygen exposed molybdenum trioxide films. *Appl. Phys. Lett.* **2010**, *96*, 243307.
(71) Chithambararaj, A.; Yogamalar, N. R.; Bose, A. C. Hydrothermally Synthesized h-MoO_3 and alpha-MoO_3 Nanocrystals: New Findings on Crystal-Structure-Dependent Charge Transport. *Cryst. Growth Des.* **2016**, *16*, 1984−1995.

DOI: 10.1021/acs.cgd.9b00646
Cryst. Growth Des. 2019, 19, 5249−5257